Metrol. Meas. Syst., Vol. 32 (2025) No. 2, pp. 1–17
DOI: 10.24425/mms.2025.154344

PAN POLSKA AKADEMIA NAUK

METROLOGY AND MEASUREMENT SYSTEMS
Index 330930, ISSN 0860-8229
www.metrology.wat.edu.pl

M&MS

A 6-DOF IN-SITU TRACKING SYSTEM-BASED KINEMATIC PARAMETERS ONLINE LEARNING METHOD FOR THE PARALLEL ROBOT

Fei Ren[1)], Zhihua Liu[2)], Chenguang Cai[2)], Ming Yang[1)], Han Zhang[2)], Zixiao Ren[2)]

1) College of Electrical Engineering, Guizhou University, 550025 Guiyang, China
2) Institute of Mechanics and Acoustic Metrology, National Institute of Metrology, 100029 Beijing, China
(✉ *liuzhihua@nim.ac.cn*)

Abstract

Kinematic parameter errors of parallel robots are affected by manufacturing errors, assembly errors, and shape errors caused by heavy loads, resulting in a gradual decrease of their kinematic accuracy. This study proposes an online learning method for the kinematic parameter errors based on a six-degree-of-freedom (6-DOF) in-situ tracking system, which achieves their online identification. This method uses six high-precision measurement legs that are embedded in the parallel robot to achieve in-situ data measurement and adopts an online learning method to identify the kinematic parameter errors. Experimental results compared with the least squares method demonstrated that the proposed method effectively achieves online identification of the kinematic parameter errors, with position and orientation accuracy improved by 85.3% and 79.2%, respectively. Moreover, it can also maintain small position deviations even under varying loads, thus sustaining the high-accuracy motion of the parallel robot.

Keywords: kinematic parameter errors, online learning, parallel robot, in-situ tracking system.

1. Introduction

Parallel robots utilize a distinct closed-loop structural design [1, 2], compared to serial mechanisms, which exhibit faster dynamic response, higher payload-to-weight ratio, and better repeatability. Consequently, parallel robots are widely utilized in the fields of manufacturing [3–5], biomedical engineering [6], and aerospace [7], which, in turn, demands higher precision performance. Due to the manufacturing errors, assembly errors, and shape errors caused by heavy loads, the kinematic parameters of parallel robots vary over time, resulting in a gradual decrease in their kinematic accuracy. Therefore, it is crucial to develop a method capable of real-time measurement, online identification, and correction of kinematic parameter errors for the parallel robot.

Currently, kinematic calibration is the primary method to enhance precision. The principle involves constructing an error function between the measured information and the control model output. Through optimization algorithms, kinematic parameters are identified to correct the

Article history: received December 6, 2024; revised February 2, 2025; accepted March 23, 2025; available online May 06, 2025.

control model. This identification process achieves error compensation. Kinematic calibration generally comprises four steps: modelling of kinematic parameter errors, measurement of pose, identification of kinematic parameter errors, and compensation of the parameter error. Based on the different measurement approaches, kinematic calibration can be further classified into three methods: external calibration, constrained calibration, and self-calibration [8]. Correspondingly, the current kinematic calibration methods of parallel mechanisms are summarized in Table 1. The measurement devices mainly include laser trackers [9–11] and vision sensors [12–15], where the laser tracker is the most commonly used. Kong *et al*. [16] utilized an API-T3 laser tracker to achieve external calibration of a 3-DOF parallel robot, Marko *et al.* [17] obtained the spatial coordinates of the robot through a stereo vision system for external calibration. Although external calibration methods can provide high-precision calibration results, the implementation process is relatively complex and easily affected by environmental factors. Li *et al.* [18] proposed a calibration method for over-constrained spatial translational parallel mechanisms, which significantly improved the calibration accuracy. However, the calibration accuracy relies on the precision and stability of the constraint conditions. Self-calibration techniques can be classified into motion constraint methods and redundant sensor methods. The former reduces the mobility of the system by fixing one or more passive joints or constraining partial degrees of freedom of the manipulator, enabling the execution of the calibration algorithm. Khalil *et al.* [19, 20] achieved self-calibration by locking the fixed passive universal joint or passive spherical joint of parallel robots. However, due to the presence of motion constraints, some parameter errors associated with the locked passive joints may become unobservable in the calibration algorithm, limiting the accuracy of the calibration. Another approach is the redundant sensor method, which utilizes excess sensors or measurement information in the system, which enable identification of kinematic parameter errors and calibration can be achieved. Zhang *et al.* [21–23] proposed using redundant encoders and additional cameras for the self-calibration of cable-driven parallel robots. However, these methods suffer from complex data processing procedures, difficulties in integrating external auxiliary devices (cameras and lasers) with the system, and are unable to monitor changes in kinematic parameter errors online.

Table 1. Summary of related works on parallel mechanism kinematic calibration.

Parallel mechanism	**Measurement device**	**Achieved accuracy (mm)**	**Identification method**
3-PRRU parallel manipulator [16]	laser tracker	0.21	*Total least-square*
Tri-pyramid robot [18]	double ball bar and 3 axes linear stage with micrometres	0.16	*Least-square*
6-DOF hybrid robot [20]	laser tracker	0.05	*Least-square Liu-estimation*
6-DOF cable-driven parallel robots [21]	camera	1.65	*Least-square*
6-DOF cable-driven parallel robots [22]	laser displacement sensors	1.40	*Genetic algorithms*
Stewart platform [23]	laser tracker	0.20	*Levenberg-Marquardt*

This study has developed an in-situ pose measurement system for a 6-DOF parallel robot. Based on this measurement system, an online learning method for identifying the kinematic parameter errors of the 6-DOF parallel robot is proposed. The method achieves online identification of the parallel robot's kinematic parameter errors through the in-situ pose measurement system and an *extended Kalman filter* (EKF) algorithm. Compared with traditional offline identification methods,

the EKF can estimate parameter changes online. The main contributions of this research include: (a) The design of a 6-DOF in-situ tracking system integrated within the parallel robot, which enables online measurement of the pose of the parallel robot. (b) Proposal of an online learning method for kinematic parameter errors, based on the 6-DOF in-situ tracking system to achieve online identification of kinematic parameter errors in the parallel robot. (c) Verification of effectiveness of the proposed method through comparative experiments, demonstrating its capability to monitor kinematic parameter errors online and maintain high kinematic accuracy of the parallel robot.

The rest of the manuscript is organized as follows: Section 2 presents a detailed description of the 6-DOF in-situ tracking system. Section 3 presents the kinematic parameter error model of the parallel robot and the online learning algorithm. Section 4 describes the kinematic calibration experiments conducted on the parallel robot. Section 5 presents the conclusions.

2. The 6-DOF in-situ tracking system

Figure 1 shows a schematic diagram of kinematic parameter errors online identification for a parallel robot based on a 6-DOF in-situ tracking system. (I) represents the processing unit, (II) denotes the parallel robot, and (III) signifies the 6-DOF in-situ tracking unit. The processing unit controls the parallel robot to perform spatial trajectory motions through a human-machine interface. The measurement legs of the 6-DOF in-situ tracking unit consist of high-precision grating rulers, sliders, reading heads, and guide rails. The measurement legs and the driving legs are connected to the same moving platform and fixed base. The guide rails move linearly in a reciprocating motion with the moving platform. This motion drives the grating rulers to move accurately thereby achieving real-time tracking of the parallel robot motion trajectory. The combination of the measuring legs with the moving platform and fixed base of the parallel robot can be considered another parallel mechanism. Through forward kinematics [24–26], the current leg length data of the six measuring legs can be converted into the actual pose of the parallel robot. The tracking system has been precisely calibrated using stereo vision technology [27]. The nominal kinematic parameters of the six measurement legs are listed in Table 2. Specifically, $\boldsymbol{h}_i = \left[h_{xi}, h_{yi}, h_{zi}\right]^T$ denotes the upper joint bearing position information, $\boldsymbol{z}_i = \left[z_{xi}, z_{yi}, z_{zi}\right]^T$ denotes the lower joint bearing position information, and $\boldsymbol{l}_{si}$ represents the initial length information of the measurement legs. Finally, the processing unit reads the tracking data. It then achieves online identification of the 42 kinematic parameter errors of the parallel robot through an online learning method based on the EKF.

Table 2. Nominal kinematic parameters of the measurement legs.

i	h_{ix}/mm	h_{iy}/mm	h_{iz}/mm	z_{ix}/mm	z_{iy}/mm	z_{iz}/mm	l_{si}/mm
1	231.600	–104.850	–127.210	728.280	41.410	108.790	1029.480
2	206.600	–148.150	–127.210	328.280	–651.410	108.790	1029.480
3	–206.600	–148.150	–127.210	–328.280	–651.410	108.790	1029.480
4	–231.600	–104.850	–127.210	–728.280	41.410	108.790	1029.480
5	–25.000	253.000	–127.210	–400.000	610.000	108.790	1029.480
6	25.000	253.000	–127.210	400.000	610.000	108.790	1029.480

3. Kinematic parameter error identification based on the online learning algorithm

3.1. Kinematic error model of the parallel robot

As shown in (II) of Fig. 1, the Hooke joints at both ends of the driving legs connect the moving platform and the fixed base. Under the drive of the servo motors, the moving platform can translate and rotate along each axis. As shown in Fig. 2, coordinate systems {D}and {J}are established on the moving platform and the fixed base of the parallel robot, respectively. Here, the coordinate system {D}serves as a local coordinate system, with its origin located at the geometric centre of the upper surface of the moving platform of the parallel robot. Meanwhile, coordinate system {J}is located on the fixed base of the parallel robot, serving as the global coordinate system for the entire system. It provides a unified reference for describing the position and motion of various components within the system, and its origin is located at the geometric centre of the upper surface of the base. $\boldsymbol{D}_i$ and $\boldsymbol{J}_i$ are the hinge connection points of the Hooke joints with the moving platform and the fixed base. The length $\boldsymbol{l}_i$ is the distance between the upper hinge point $\boldsymbol{d}_i = [d_{xi}, d_{yi}, d_{zi}]^T$ and the lower hinge point $\boldsymbol{j}_i = [j_{xi}, j_{yi}, j_{zi}]^T$.

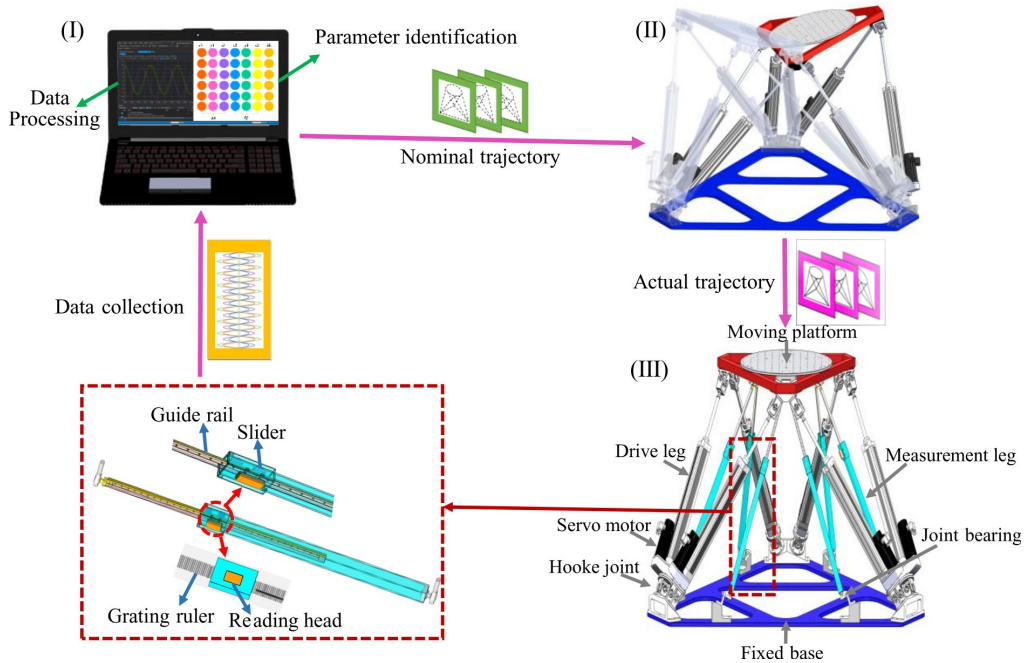

Fig. 1. Schematic diagram of kinematic parameter error online identification in parallel robots: (I) processing unit, (II) parallel robot, (III) 6-DOF in-situ tracking unit.

The kinematic parameter errors of the aforementioned parallel mechanism include the hinge error of the moving platform $\delta\boldsymbol{d}_i$, the hinge error of the fixed base $\delta\boldsymbol{j}_i$, and the length error of the driving leg $\delta\boldsymbol{l}_i$. By compensating for these 42 kinematic parameter errors, the accuracy of the parallel robot can be ensured across various motion trajectories, which enables precise control and high repeatability. As illustrated in Fig. 2(b), the closed-loop vector equation for the i^{th} path within the kinematic error model is

$$\boldsymbol{l}_i\boldsymbol{n}_i = \boldsymbol{h} + \boldsymbol{R}_\psi\boldsymbol{d}_i - \boldsymbol{j}_i, \tag{1}$$

Metrol. Meas. Syst., Vol. 32 (2025), No. 2, pp. 1–17
DOI: 10.24425/mms.2025.154344

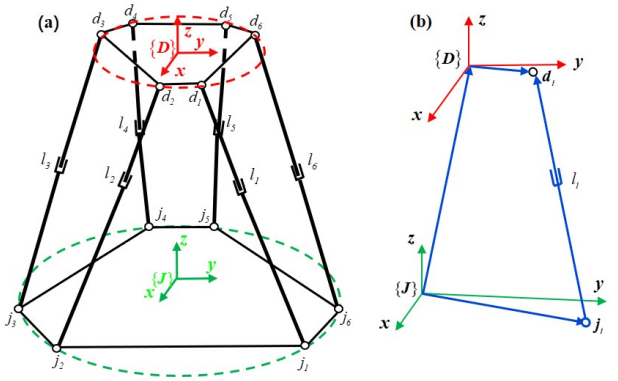

Fig. 2. Kinematic analysis of the parallel robot: (a) kinematic scheme, (b) closed-loop vector of $\boldsymbol{l_i}$.

where $\boldsymbol{n}_i$ is defined as the unit vector of $\boldsymbol{l}_i$, and $\boldsymbol{h}$ denotes the position vector oriented from the origin of the base coordinate system to the origin of the moving platform coordinate system. Additionally, $\boldsymbol{R}_\psi$ represents the rotation matrix involved. The left and right of (1) are fully differentiated to obtain the closed-loop differential equations:

$$l_i\delta\boldsymbol{n}_i + \boldsymbol{n}_i\delta l_i = \delta\boldsymbol{h} + \delta\boldsymbol{R}_\psi\boldsymbol{d}_i + \boldsymbol{R}_\psi\delta\boldsymbol{d}_i - \delta\boldsymbol{j}_i, \tag{2}$$

$$l_i\delta\boldsymbol{n}_i + \boldsymbol{n}_i\delta l_i = \delta\boldsymbol{h} + \omega\times\boldsymbol{R}_\psi\boldsymbol{d}_i + \boldsymbol{R}_\psi\delta\boldsymbol{d}_i - \delta\boldsymbol{j}_i, \tag{3}$$

where the rotation matrix $\boldsymbol{R}_\psi$ is usually determined by Euler angles $\alpha-\beta-\gamma$, with the detailed rotation definitions provided in the Appendix, the relation between ω and Euler angles is

$$\boldsymbol{\omega} = \boldsymbol{T}\delta\boldsymbol{\theta}, \tag{4}$$

where the $\boldsymbol{T}$ matrix represents the conversion between the angle ω in radians and the angular velocity $\delta\theta$, $\boldsymbol{T}$ and $\boldsymbol{R}_\psi$ can be expressed as

$$\boldsymbol{T} = \begin{bmatrix} c\beta c\gamma & -s\gamma & 0 \\ s\gamma c\beta & c\gamma & 0 \\ -s\beta & 0 & 1 \end{bmatrix} \quad \boldsymbol{R_\psi} = \begin{bmatrix} c\beta c\gamma & s\alpha s\beta c\gamma - s\gamma c\alpha & s\beta c\alpha c\gamma + s\alpha s\gamma \\ s\gamma c\beta & s\alpha s\beta s\gamma + c\alpha c\gamma & s\beta s\gamma c\alpha - s\alpha c\gamma \\ -s\beta & s\alpha c\beta & c\alpha c\beta \end{bmatrix}, \tag{5}$$

where $\boldsymbol{c}$ and $\boldsymbol{s}$ represent cos and sin, respectively. When we substitute (4) into (3), and then multiply both sides by $\boldsymbol{n}_i^T$, we get

$$\boldsymbol{n}_i^T l_i\delta\boldsymbol{n}_i + \boldsymbol{n}_i^T\boldsymbol{n}_i\delta l_i = \boldsymbol{n}_i^T\delta\boldsymbol{h} + \boldsymbol{n}_i^T(\boldsymbol{T}\delta\theta)\times\boldsymbol{R_\psi}\boldsymbol{d}_i + \boldsymbol{n}_i^T\boldsymbol{R_\psi}\delta\boldsymbol{d}_i - \boldsymbol{n}_i^T\delta\boldsymbol{j}_i, \tag{6}$$

where $\boldsymbol{n}_i^T l_i\delta\boldsymbol{n}_i = 0$, $\boldsymbol{n}_i^T\boldsymbol{n}_i\delta l_i = \delta l_i$, and then

$$\delta l_i = \boldsymbol{n}_i^T\delta\boldsymbol{h} + (\boldsymbol{R}_\psi\boldsymbol{d}_i\times\boldsymbol{n}_i)^T\boldsymbol{T}\delta\theta + \boldsymbol{n}_i^T\boldsymbol{R}_\psi\delta\boldsymbol{d}_i - \boldsymbol{n}_i^T\delta\boldsymbol{j}_i, \tag{7}$$

$$\begin{bmatrix} \boldsymbol{n}_i^T & (\boldsymbol{R}_\psi\boldsymbol{d}_i\times\boldsymbol{n}_i)^T\boldsymbol{T} \end{bmatrix}\begin{bmatrix} \delta\boldsymbol{h} \\ \delta\boldsymbol{\theta} \end{bmatrix} = \begin{bmatrix} \boldsymbol{n}_i^T & -\boldsymbol{n}_i^T\boldsymbol{R}_\psi & 1 \end{bmatrix}\begin{bmatrix} \delta\boldsymbol{j}_i \\ \delta\boldsymbol{d}_i \\ \delta l_i \end{bmatrix}, \tag{8}$$

$$\delta\boldsymbol{E} = \boldsymbol{J}_p\delta\boldsymbol{M}, \tag{9}$$

where $\delta\boldsymbol{E} = [\delta\boldsymbol{h}, \delta\theta]^T \in \mathbf{R^{6\times1}}$ represents the pose error vector, which indicates errors in position and orientation. Meanwhile, $\delta\boldsymbol{M} = [\delta\boldsymbol{j}_1^T, \delta\boldsymbol{d}_1^T, \delta l_1 \ldots \delta\boldsymbol{j}_6^T, \delta\boldsymbol{d}_6^T, \delta l_6]^T$, $\delta\boldsymbol{M} \in \mathbf{R^{42\times1}}$ represents 42

kinematic parameter errors, which include 6 leg length errors and 36 positional errors of the Hooke joints. $\boldsymbol{J}_P$ denotes the error Jacobian matrix, with $\boldsymbol{J}_P = \boldsymbol{J}_r \boldsymbol{J}_s$, and $\boldsymbol{J}_P \in \mathbf{R}^{\mathbf{6\times 42}}$, the definition of the error Jacobian matrix is detailed in the Appendix:

$$\boldsymbol{J}_r = \begin{bmatrix} \boldsymbol{n}_1^T & (\boldsymbol{R}_\psi \boldsymbol{d}_1 \times \boldsymbol{n}_1)^T \boldsymbol{T} \\ \vdots & \vdots \\ \boldsymbol{n}_6^T & (\boldsymbol{R}_\psi \boldsymbol{d}_6 \times \boldsymbol{n}_6)^T \boldsymbol{T} \end{bmatrix}^{-1}, \tag{10}$$

$$\boldsymbol{J}_s = \begin{bmatrix} \boldsymbol{n}_1^T & -\boldsymbol{n}_1^T \boldsymbol{R}_\psi & 1 & \cdots & 0 & 0 & 0 \\ \vdots & \vdots & \vdots & \ddots & \vdots & \vdots & \vdots \\ 0 & 0 & 0 & \cdots & \boldsymbol{n}_6^T & -\boldsymbol{n}_6^T \boldsymbol{R}_\psi & 1 \end{bmatrix}. \tag{11}$$

The $\boldsymbol{j}_i$ and $\boldsymbol{d}_i$ can be expressed as

$$\boldsymbol{j}_i = [j_{xi}\ j_{yi}\ j_{zi}]^T, \quad i = \{1, 2, ..., 6\}, \tag{12}$$

$$\boldsymbol{d}_i = [d_{xi}\ d_{yi}\ d_{zi}]^T, \quad i = \{1, 2, ..., 6\}. \tag{13}$$

The online learning algorithm discussed in the subsequent section will utilize (9) for the precise estimation of these parameters.

3.2. Online learning algorithm

The EKF is an online learning algorithm that relies on the assumption of *independent and identically distributed* (IID) data. The EKF algorithm can accurately and effectively perform state estimation and prediction only when the IID assumption is satisfied. In this study, the position points of the upper Hooke joints (denoted as $\boldsymbol{d}_i$) in the 6-DOF parallel robot are defined as fixed points in the local coordinate system, with these positions determined by the pose of the moving platform. Therefore, the position points $\boldsymbol{d}_i$ of the upper Hooke joints and the leg lengths l_i can be considered mutually independent. This ensures that the error model satisfies the IID assumption required by the EKF algorithm. In this framework, the kinematic parameter errors $\delta\boldsymbol{M}$ and the pose error $\delta\boldsymbol{E}$ are treated as the state and observation variables of the EKF, denoted respectively by $\boldsymbol{X} = \delta\boldsymbol{M}$ and $\boldsymbol{Y} = \delta\boldsymbol{E}$. The algorithm includes two main phases: prediction and update. During the prediction phase, the state vector $\boldsymbol{X}$ and the prediction covariance matrix $\boldsymbol{P}$ are governed by the following linear differential equations, based on (9), with $\boldsymbol{X}_{k-1|k-1} = \delta\boldsymbol{M}$, and $\boldsymbol{J}_k = \boldsymbol{J}_P$. The state transition equation of EKF is

$$\boldsymbol{K}_{k|k-1} = \boldsymbol{K}_{k-1|k-1}, \tag{14}$$

$$\boldsymbol{P}_{k|k-1} = \boldsymbol{P}_{k-1|k-1} + \boldsymbol{Q}_{k-1}, \tag{15}$$

where $\boldsymbol{X}_{k-1|k-1} \in \mathbf{R}^{\mathbf{42\times 1}}$ represents the prior estimate at the $(k-1)^{\text{th}}$, and $\boldsymbol{X}_{k|k-1}$ denotes the posterior estimate. Additionally, $\boldsymbol{P}_{k-1|k-1} \in \mathbf{R}^{\mathbf{42\times 42}}$ signifies the covariance matrix, and $\boldsymbol{Q}_{k-1} \in \mathbf{R}^{\mathbf{42\times 42}}$ is the covariance matrix of the system noise.

The measurement equation of the EKF is

$$\boldsymbol{Y}_k = \boldsymbol{J}_k \boldsymbol{K}_k + \boldsymbol{E}_k, \tag{16}$$

where $\boldsymbol{Y}_k \in \mathbf{R}^{\mathbf{6\times 1}}$ is the pose error vector, and $\boldsymbol{E}_k \in \mathbf{R}^{\mathbf{6\times 1}}$ is the measurement noise vector.

The Kalman gain can be expressed as

$$\boldsymbol{K}_k = \boldsymbol{P}_{k|k-1}\boldsymbol{J}_k^T \left(\boldsymbol{J}_k\boldsymbol{P}_{k|k-1}\boldsymbol{J}_k{}^T + \boldsymbol{R}_k\right)^{-1}, \tag{17}$$

where $\boldsymbol{K}_k \in \mathbf{R}^{42\times 6}$ is the gain matrix, and $\boldsymbol{R}_k = \boldsymbol{E}\left(\boldsymbol{E}_k\boldsymbol{E}_k^T\right) \in \mathbf{R}^{6\times 6}$ is the measurement noise covariance matrix.

The state update equation and the covariance update equation are as follows:

$$\boldsymbol{K}_{k|k} = \boldsymbol{X}_{k|k-1} + \boldsymbol{K}_k\left(\boldsymbol{Y}_k - \mathbf{J}_k\boldsymbol{K}_{k|k-1}\right), \tag{18}$$

$$\boldsymbol{P}_{k|k} = \left(\boldsymbol{I} - \boldsymbol{K}_k\boldsymbol{J}_k\right)\boldsymbol{P}_{k|k-1}, \tag{19}$$

where $\boldsymbol{I} \in \mathbf{R}^{42\times 42}$ is the identity matrix.

During the online identification process of kinematic parameter errors, the computational complexity of the algorithm directly affects its real-time performance. Consequently, a detailed analysis of the computational complexity of the EKF was conducted, with the specific results summarized in Table 3.

Table 3. Computational complexity of the EKF.

Equation	Complexity	×/÷	+/−
$\boldsymbol{P}_{k\|k-1} = \boldsymbol{P}_{k-1\|k-1} + \boldsymbol{Q}_{k-1}$	$\boldsymbol{O}(n^2)$	0	1764
$\boldsymbol{Y}_k = \boldsymbol{J}_k\boldsymbol{X}_k + \boldsymbol{E}_k$	$\boldsymbol{O}(mn)$	252	252
$\boldsymbol{K}_k = \boldsymbol{P}_{k\|k-1}\boldsymbol{J}_k^T(\boldsymbol{J}_k\boldsymbol{P}_{k\|k-1}\boldsymbol{J}_k^T + \boldsymbol{R}_k)^{-1}$	$\boldsymbol{O}(mn^2 + m^2n + m^3)$	24408	21924
$\boldsymbol{X}_{k\|k} = \boldsymbol{X}_{k\|k-1} + \boldsymbol{K}_k(\boldsymbol{Y}_k - \boldsymbol{J}_k\boldsymbol{X}_{k\|k-1})$	$\boldsymbol{O}(mn)$	504	504
$\boldsymbol{P}_{k\|k} = (\boldsymbol{I} - \boldsymbol{K}_k\boldsymbol{J}_k)\boldsymbol{P}_{k\|k-1}$	$\boldsymbol{O}(n^3 + mn^2)$	84672	84420

Table 3 quantifies the computational cost of the EKF method using the number of multiplication/division (×/÷) and addition/subtraction (+/−) operations as metrics. Among these, the calculation of the Kalman gain and the covariance update account for the majority of the computational overhead. However, the computational cycle remains shorter than that of the control system, meeting the requirements for online identification of kinematic parameter errors in the parallel robot.

During each iteration, the covariance matrices $\boldsymbol{Q}$ and $\boldsymbol{R}$ of the EKF are iteratively updated [28]. The accuracy of the measurement devices can be used as the initial estimate for the covariance matrix $\boldsymbol{R}$. Based on the aforementioned error model and the EKF algorithm, the identification process of the kinematic parameter errors for the parallel robot is shown in Fig. 3. The detailed steps of this process include:

Step 1: To determine the actual pose $\boldsymbol{P}_v$ of the parallel robot, we first collect length measurements from the six grating rulers while the robot is held in a static pose. These leg length values are then used as inputs for forward kinematic calculations using the Newton–Raphson method [29]. This process converts the leg length data into the corresponding pose, represented by $\boldsymbol{P}_v$.

Step 2: Calculation of the difference between the current nominal pose $\boldsymbol{P}_m$ and the actual pose $\boldsymbol{P}_v$, as well as the error Jacobian matrix $\boldsymbol{J}_k$ under the current nominal pose $\boldsymbol{P}_m$.

Step 3: Inputting the pose error $\boldsymbol{P}_m - \boldsymbol{P}_v$ and the error Jacobian matrix $\boldsymbol{J}_k$ into the EKF to achieve online identification of the 42 kinematic parameter errors.

Step 4: After identifying the error $\delta\boldsymbol{v}$ in the kinematic parameters, adding the error value $\delta\boldsymbol{v}$ to the nominal parameter $\boldsymbol{v}$ thereby updating the kinematic model of the parallel robot for calibration.

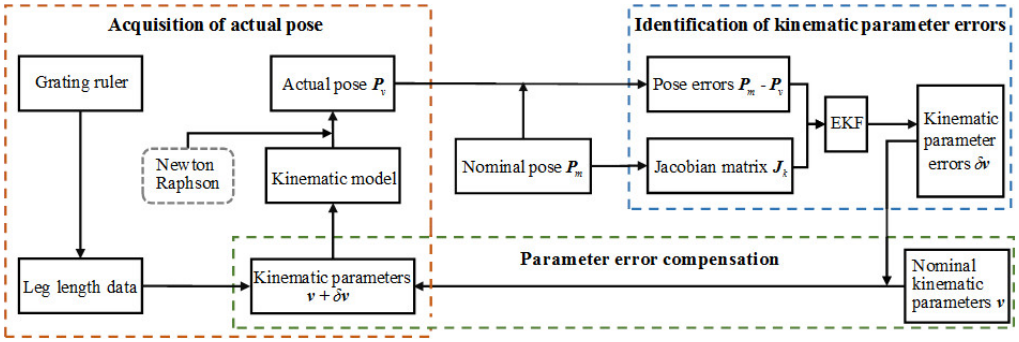

Fig. 3. Calibration procedure of the proposed method.

4. Experimental validation and results

4.1. Experimental system

To verify the feasibility of the proposed online measurement method based on the 6-DOF in-situ tracking system and the online learning algorithm described in Section 3, a kinematic calibration experiment was designed using a Stewart platform. The experimental setup is shown in Fig. 4. Figure 4(a) presents the Beckhoff controller, which comprises an embedded control module and a power module. This controller connects to the motion control software TwinCAT3.0 to achieve system control and data transmission. Figure 1(b) illustrates the Renishaw reading head. Its working principle involves emitting a light beam with a high-intensity light source, which is converted into parallel light by a collimating lens. The beam is then separated with a beam splitter and directed onto a grating. The grating modulates the beam which alters its path and intensity. The modulated beam is focused with a detection lens onto a high-speed custom detection array

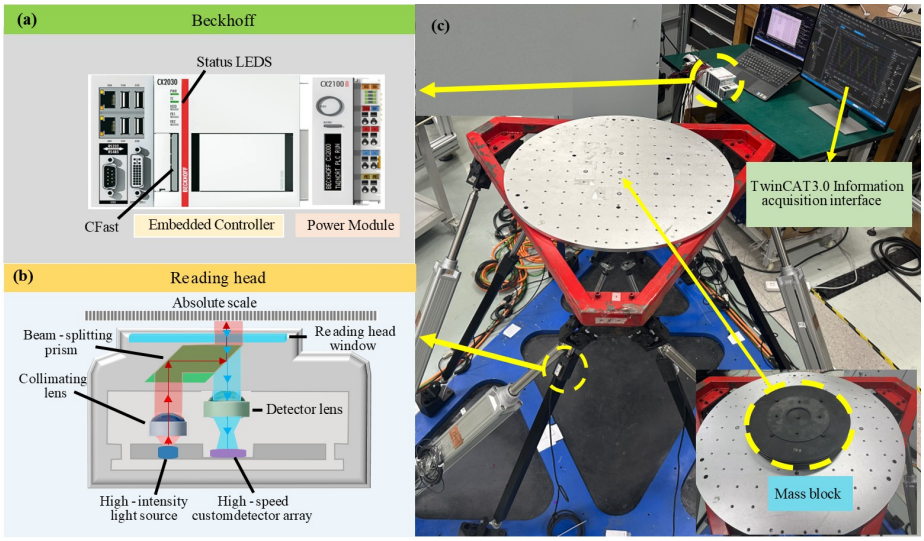

Fig. 4. Experimental setup: (a) controller module, (b) internal structure of the reading head, (c) motion generation device.

which converts the light signal into an electrical signal. After signal processing, the system outputs precise position information. The resolution of the grating ruler is 50 nm, and the measurement range is –276 to 318 mm. Figure 4(c) displays the Stewart platform, with displacement ranges along the x, y, and z axes of –200 to 200 mm and orientation ranges of –20° to 20°.

The experiment consists of two parts: a static pose comparison and a dynamic trajectory comparison. Throughout the load variation process, the EKF was employed to perform online identification of kinematic parameter errors. Subsequently, the Stewart motion platform was calibrated using the identified parameters. The calibration results obtained from the EKF were then compared and analysed against those derived from the least squares method. During the identification process using the EKF, the system noise covariance matrix $\boldsymbol{Q}$ was initialized as $10^{-5} \times \boldsymbol{I}_{42\times42}$, and the measurement noise covariance matrix $\boldsymbol{R}$ was initialized as $4 \times 10^{-2} \times \boldsymbol{I}_{6\times6}$.

Additionally, prior to conducting the experiments, a comparative study was performed with a high-precision binocular vision instrument (AICON MoveInspect XR) to validate the accuracy of the proposed measurement device. The experimental results showed that, compared to the binocular vision instrument, the proposed measurement device had an average position error of 0.036 mm and an average orientation error of 0.022.

4.2. Comparison of static poses

The EKF was applied to identify the kinematic parameter errors of the Stewart platform, according to the identification process depicted in Fig. 3. The identified kinematic parameter errors under the no-load conditions are presented in Fig. 5.

Figure 5 shows six subplots, each with seven curves representing the kinematic parameter errors for each drive leg, including errors in the positions of the upper and lower Hooke joints and the lengths of the drive legs. Additionally, Fig. 5 demonstrates the rapid convergence of the EKF in identifying kinematic parameter errors. Table 4 lists the 42 kinematic parameter errors identified by both the EKF and the least squares method under no-load conditions.

As the primary external disturbance, the payload can cause variations in the kinematic parameter errors of parallel robots, which significantly affects the kinematic accuracy [30, 31]. Traditional methods were incapable of monitoring the variations of kinematic parameter errors online. To address this, the Stewart platform was first calibrated using the data from Table 4. Then, a payload was applied, and the variations of kinematic parameter errors under payload conditions were identified using the EKF method. The experimental results are shown in Fig. 6.

Table 4. Identified kinematic parameter errors (mm).

	LS							**EKF**						
Leg *i*	δj_{xi}	δj_{yi}	δj_{zi}	δd_{xi}	δd_{yi}	δd_{zi}	δl_i	δj_{xi}	δj_{yi}	δj_{zi}	δd_{xi}	δd_{yi}	δd_{zi}	δl_i
1	0.146	–1.560	–2.819	–2.564	–2.675	0.006	–0.413	0.118	–1.374	–2.660	–2.285	–3.207	0.281	–0.186
2	–0.237	–0.160	–2.762	–3.379	–2.941	–0.190	0.276	0.427	1.754	–0.219	–3.148	–3.205	0.266	–2.631
3	0.018	–0.071	–2.398	–3.296	2.561	–0.017	0.686	0.140	–0140	–2.243	–3.251	2.046	–0.463	–0.143
4	1.348	–1.765	3.271	–1.041	3.339	0.287	–1.384	0.195	–0.484	1.876	–1.949	3.756	–0.789	–0.531
5	1.574	–0.254	3.774	2.361	0.723	0.949	–1.788	–0.472	–0.397	1.514	1.459	1.399	0.378	0.126
6	0.225	–1.046	–2.167	2.033	–0.928	0.977	0.746	–0.797	–2.545	–0.861	2.745	–0.729	–0.351	–2.352

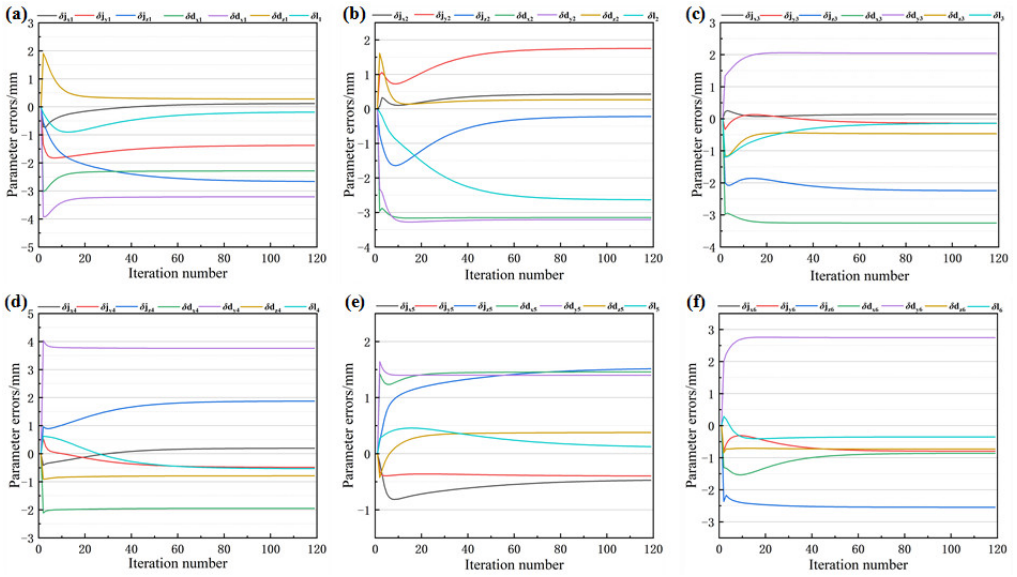

Fig. 5. Identification of kinematic parameter errors with the EKF algorithm.

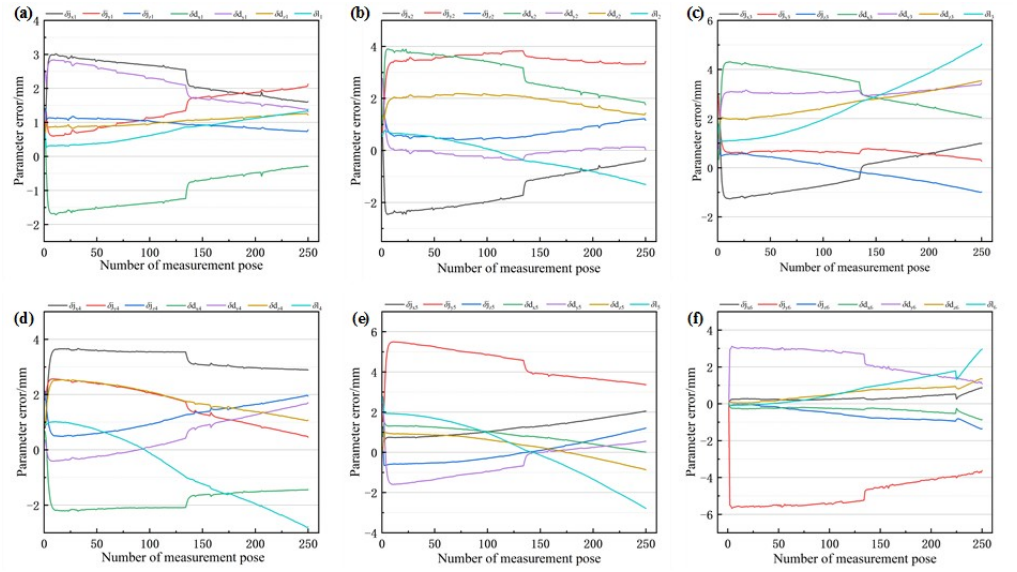

Fig. 6. Online identification of kinematic parameter errors.

As shown in Fig. 6, the kinematic parameter errors of the Stewart platform changed significantly after the payload was applied. To address the impact of variations in kinematic parameter errors on the kinematic accuracy of the Stewart platform, calibration experiments were conducted under payload conditions of 20 kg and 40 kg, respectively. The experimental results are presented in Fig. 7 and Table 5.

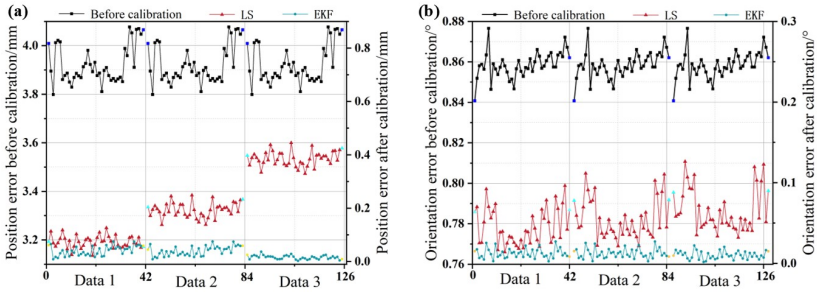

Fig. 7. Pose errors before and after calibration: (a) position error, (b) orientation error.

Table 5. Comparison of pose errors before and after kinematic calibration.

Pose errors	Before calibration	After calibration					
		LS			EKF		
		Data1	Data2	Data3	Data1	Data2	Data3
Position (mm)	3.9243	0.0734	0.1926	0.3854	0.0403	0.0398	0.0156
Orientation (°)	0.8524	0.0459	0.0552	0.0661	0.0124	0.0123	0.0103

In Fig. 7, since the least squares method was unable to identify the variations in kinematic parameter errors, only the initial calibration under no-load conditions was performed. In Table 5, Data1 represents the calibration data under no-load conditions, Data2 represents the calibration data with a 20 kg load, and Data3 represents the calibration data with a 40 kg load. Before the calibration, the Stewart platform had a position error of 3.9243 mm and an orientation error of 0.8524°. After the calibration, the least squares method increased the average position error from 0.0734 mm to 0.1926 mm, and eventually reached 0.3854 mm. The mean value of the position errors across the three trials was 0.2171 mm. The average orientation error increased from 0.0459° to 0.0552°, and eventually reached 0.0661°. The mean value of the orientation errors across the three trials was 0.0557°. In contrast, the proposed method reduced the average position error from 0.0403 mm to 0.0398 mm, and eventually lowered it to 0.0156 mm. The mean value of the position errors across the three trials was 0.0319 mm. The average orientation error decreased from 0.0124° to 0.0123°, and eventually dropped to 0.0103°. The mean value of the orientation errors across the three trials was 0.0116°. Compared to the least squares method, the proposed approach improved position accuracy and orientation accuracy by 85.3% and 79.2%, respectively, in terms of average position and orientation errors over three calibrations.

4.3. Comparison of dynamic trajectories

The aforementioned experimental results clearly demonstrated that the motion accuracy of the Stewart platform gradually decreased over time when the traditional calibration method was applied. To more intuitively monitor this change, a circular trajectory experiment was specifically designed. Under the application of an external load, the deviation of the parallel robot's motion trajectory was observed, while the proposed kinematic calibration method was employed and compared with the traditional calibration method. All experimental settings were kept consistent with those of the static pose comparison experiment to ensure the uniformity of experimental conditions and the reliability of the results thereby enabling a more accurate evaluation of the performance differences between the different calibration methods.

Figure 8 clearly illustrates the variation of the Stewart platform trajectory before and after the calibration. After the calibration using the least squares method, the actual motion trajectory diverged from the theoretical trajectory due to external loads. To show this deviation data more clearly, the position deviations between the actual and theoretical trajectories are represented in a polar coordinate system, as shown in Fig. 9. The corresponding data are summarized in Table 6.

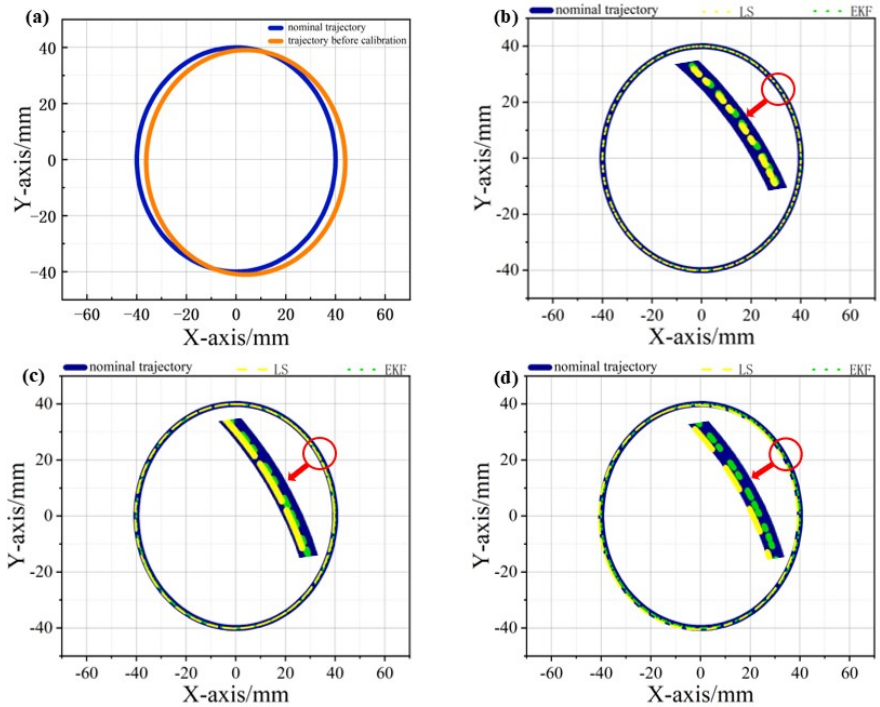

Fig. 8. Comparison of circular trajectories before and after the calibration: (a) trajectory comparison before the calibration, (b)–(d) trajectory comparison after the calibration.

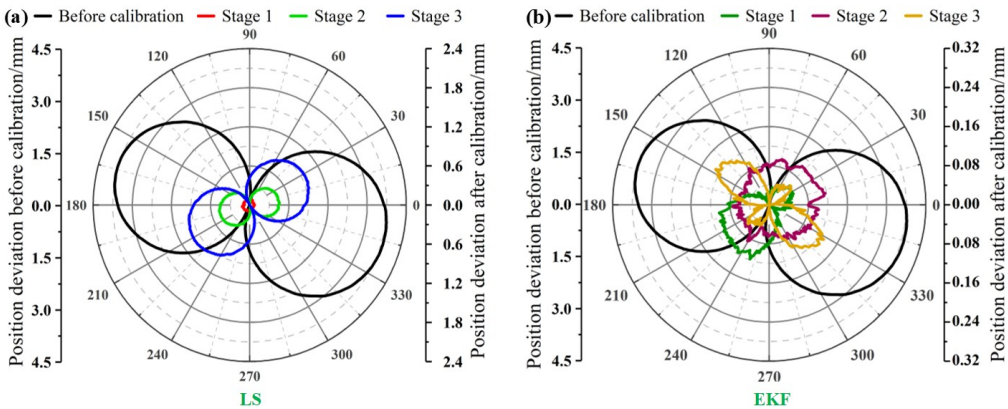

Fig. 9. Positional deviations before and after the calibration: (a) the positional deviations based on the LS, (b) the positional deviations based on the EKF.

Table 6 illustrates the influence of load on the kinematic accuracy of the Stewart platform. After the calibration using the least squares method, the position deviation increased from 0.0771 mm to 0.2937 mm, and ultimately reached 0.6223 mm, with an average position deviation of 0.3310 mm. In contrast, the proposed method consistently maintained the required kinematic accuracy, with position deviations were 0.0515 mm, 0.0769 mm, and 0.0564 mm, with an average position deviation of 0.0616 mm. Compared to the least squares method, the proposed method reduced the average position deviation by 81.4%, across three trials.

Table 6. Comparison of deviation before and after the kinematic calibration.

Deviation	**Trajectory**	**Before the calibration**	**After the calibration**					
			LS			**EKF**		
			Stage 1	**Stage 2**	**Stage 3**	**Stage 1**	**Stage 2**	**Stage 3**
Position deviation (mm)	Circle	2.5334	0.0771	0.2937	0.6223	0.0515	0.0769	0.0564

4.4. Discussion

In the static pose comparison experiment, Fig. 5 demonstrates the rapid convergence of the EKF in identifying kinematic parameter errors. The applied load on the motion platform of the Stewart platform caused gradual changes in the 42 kinematic parameter errors, as shown in Fig. 6. The co-axial error curves on each drive leg were symmetrical, whereas the error curves for the lengths of the six legs did not exhibit the same variation trend. This discrepancy was likely because the load was not centred on the motion platform. Figure 7 illustrates the variation of pose errors during the continuous change of kinematic parameter errors in the Stewart platform. As the least squares method fails to identify the kinematic parameter errors of the Stewart platform online, the pose error gradually increases. Compared to the least squares method, the EKF not only corrected errors using observations (*e.g.*, pose errors) but also dynamically updated state estimations through an error prediction model. In contrast, the method proposed in this study effectively monitored the changes in kinematic parameter errors, which enabled the pose error to decrease progressively. The position error decreased from an initial 0.0403 mm to 0.0398 mm and finally reached 0.0156 mm. Simultaneously, the orientation error also reduced from 0.0124° to 0.0123° and ultimately decreased to 0.0103°.

To clearly observe the influence of kinematic parameter error variations on the motion trajectory, a dynamic trajectory experiment was designed. As clearly shown in Fig. 8, under the influence of external loads, the actual motion trajectory of the Stewart platform gradually deviated from the predetermined nominal trajectory. In contrast, the motion trajectory obtained using the proposed method highly coincided with the nominal trajectory. Furthermore, by comparing Fig. 9(a) and 9(b), it was observed that the smoothness of the compensated trajectory was suboptimal, primarily due to external disturbances.

5. Conclusions

In this study an in-situ measurement system for a 6-DOF parallel robot was developed, which enables online pose measurement. Based on this system, an online learning method for kinematic parameter errors of the 6-DOF parallel robot was proposed. This method utilized the

measurement system and the EKF algorithm to obtain current kinematic parameter errors of the parallel robot online. To validate the effectiveness of the proposed method, calibration experiments were conducted and compared with the traditional least squares method. Through the analysis of experimental results, the following conclusions are drawn:

1. Compared to traditional measurement methods, the proposed approach enabled online measurement of the pose of the parallel robot and was more easily integrated with the parallel robot system. Moreover, this method demonstrated significant advantages in terms of data processing.
2. This method enabled online monitoring of the variations in kinematic parameter errors of the parallel robot thereby ensuring its kinematic accuracy.
3. The experimental results demonstrated that the proposed method effectively identified the kinematic parameter errors of the Stewart platform online. In the calibration experiments, compared to the least squares method, the proposed method significantly improved the positioning accuracy and orientation accuracy by 85.3% and 79.2%, respectively, for static poses. In addition, it reduced positional deviations by 81.4%, for dynamic trajectories. The experimental results further validate that the proposed method effectively maintains high kinematic accuracy under varying external loads.

Future work will focus on further optimizing the online learning algorithm to improve computational efficiency and enhance disturbance resistance. Additionally, efforts will be made to extend the application of this method to various types of parallel robots, exploring broader application prospects.

6. Acknowledgements

This work was supported part by the National Natural Science Foundation of China (52075512, 62203132, 52265066,); Fundamental Research Funds for the National Institute of Metrology of China (No. AKYZD2302); the National Key R&D Program of China (2021YFF 0600103, 2022YFF0609400); the Youth Science and Technology Talents Development Project of Guizhou Education Department (No. Qianjiaohe KY [2022] 138); the Doctor Foundation Project of Guizhou University (No. GDRJ [2020]30).

7. Appendix

In this study, Euler angles (RPY) are used to represent the orientation of the parallel mechanism due to their clear physical interpretation, which enables an intuitive description of the mechanism's rotation about three mutually perpendicular spatial axes: roll, pitch, and yaw. Specifically, roll represents rotation around the x-axis, pitch represents rotation around the y-axis, and yaw represents rotation around the z-axis. The rotation sequence of the Euler angle transformation is as follows:

$$\boldsymbol{R}_{\psi} = RPY(\alpha, \beta, \gamma) = \boldsymbol{R}(z, \gamma)\boldsymbol{R}(y, \beta)\boldsymbol{R}(x, \alpha). \tag{20}$$

The rotation sequence first involves a rotation by an angle γ around the z-axis, followed by a rotation by an angle β around the y-axis, and finally a rotation by an angle α around the x-axis.

The corresponding rotation matrix expressions are as follows:

$$\boldsymbol{R}(z,\gamma) = \begin{bmatrix} c\gamma & -s\gamma & 0 \\ s\gamma & c\gamma & 0 \\ 0 & 0 & 1 \end{bmatrix} \quad \boldsymbol{R}(y,\beta) = \begin{bmatrix} c\beta & 0 & s\beta \\ 0 & 1 & 0 \\ -s\beta & 0 & c\beta \end{bmatrix} \quad \boldsymbol{R}(x,\alpha) = \begin{bmatrix} 1 & 0 & 0 \\ 0 & c\alpha & -s\alpha \\ 0 & s\alpha & c\alpha \end{bmatrix}. \tag{21}$$

The rotation matrix is utilized to describe the rotational state of the moving platform relative to the fixed platform. Additionally, during the coordinate transformation process, it facilitates the conversion of points on the moving platform from the local coordinate system to the global coordinate system.

In the kinematic error modelling of the Stewart platform, the kinematic parameter errors primarily include the drive leg length errors, the centre point position errors of the upper Hooke joint, and the centre point position errors of the lower Hooke joint. The error Jacobian matrix is derived by taking partial derivatives of the Stewart platform's kinematic equations, and it is used to describe the relationship between the platform's pose errors and kinematic parameter errors.

References

[1] Furqan, M., Suhaib, M., & Ahmad, N. (2017). Studies on Stewart platform manipulator: A review. *Journal of Mechanical Science and Technology*, 31(9), 4459–4470. https://doi.org/10.1007/s12206-017-0846-1

[2] Patel, Y. D., & George, P. M. (2012). Parallel Manipulators Applications – A Survey. *Modern Mechanical Engineering*, *02*(03), 57–64. https://doi.org/10.4236/mme.2012.23008

[3] Huang, T., Zhao, D., Yin, F., Tian, W., & Chetwynd, D. G. (2018). Kinematic calibration of a 6-DOF hybrid robot by considering multicollinearity in the identification Jacobian. *Mechanism and Machine Theory*, 131, 371–384. https://doi.org/10.1016/j.mechmachtheory.2018.10.008

[4] Song, Y., Zhang, J., Lian, B., & Sun, T. (2016). Kinematic calibration of a 5-DoF parallel kinematic machine. *Precision Engineering*, *45*, 242–261. https://doi.org/10.1016/j.precisioneng.2016.03.002

[5] Huang, P., Wang, J., Wang, L., & Yao, R. (2011). Identification of structure errors of 3-PRS-XY mechanism with Regularization method. *Mechanism and Machine Theory*, *46*(7), 927–944. https://doi.org/10.1016/j.mechmachtheory.2011.02.006

[6] Zhang, N., Huang, P., & Li, Q. (2017). Modeling, design and experiment of a remote-center-of-motion parallel manipulator for needle insertion. *Robotics and Computer-Integrated Manufacturing*, *50*, 193–202. https://doi.org/10.1016/j.rcim.2017.09.014

[7] Sun, T., Song, Y., Dong, G., Lian, B., & Liu, J. (2012). Optimal design of a parallel mechanism with three rotational degrees of freedom. *Robotics and Computer-Integrated Manufacturing*, *28*(4), 500–508. https://doi.org/10.1016/j.rcim.2012.02.002

[8] Hu, Y., Gao, F., Zhao, X., Wei, B., Zhao, D., & Zhao, Y. (2018). Kinematic calibration of a 6-DOF parallel manipulator based on identifiable parameters separation (IPS). *Mechanism and Machine Theory*, *126*, 61–78. https://doi.org/10.1016/j.mechmachtheory.2018.03.019

[9] Yang, L., Liao, R., Lin, J., Sun, B., Wang, Z., Keogh, P., & Zhu, J. (2019). Enhanced 6D measurement by integrating an Inertial Measurement Unit (IMU) with a 6D sensor unit of a laser tracker. *Optics and Lasers in Engineering*, *126*, 105902. https://doi.org/10.1016/j.optlaseng.2019.105902

[10] Yang, Q., Cai, C., Yang, M., Kong, M., Liu, Z., & Liang, F. (2022). Dynamic tilt testing of MEMS inclinometers based on conical motions. *Metrology and Measurement Systems*, Vol. 30 (2023) No. 1, 31–47. https://doi.org/10.24425/mms.2023.144398

[11] Ye, T., Liu, Z., Cai, C., Bao, F., Xu, F., & Lian, X. (2024). A novel ultra-low-frequency micro-vibration calibration method based on virtual pendulum motion trajectories of the Stewart platform. *Metrology and Measurement Systems*, Vol. 31 (2024) No. 2, 323–338. https://doi.org/10.24425/mms.2024.149695

[12] Fu, L., Liu, Z., Cai, C., Tao, M., Yang, M., & Huang, H. (2023). Joint space-based optimal measurement configuration determination method for Stewart platform kinematics calibration. *Measurement*, *211*, 112646. https://doi.org/10.1016/j.measurement.2023.112646

[13] Fu, L., Yang, M., Liu, Z., Tao, M., Cai, C., & Huang, H. (2022). Stereo vision-based Kinematic calibration method for the Stewart platforms. *Optics Express*, *30*(26), 47059. https://doi.org/10.1364/oe.479597

[14] Yang, M., Wang, Y., Liu, Z., Zuo, S., Cai, C., Yang, J., & Yang, J. (2021). A monocular vision-based decoupling measurement method for plane motion orbits. *Measurement*, *187*, 110312. https://doi.org/10.1016/j.measurement.2021.110312

[15] Zhu, X., Liu, Z., Cai, C., Yang, M., Zhang, H., Fu, L., & Zhang, J. (2024). Deep learning-based predicting and compensating method for the pose deviations of parallel robots. *Computers & Industrial Engineering*, *191*, 110179. https://doi.org/10.1016/j.cie.2024.110179

[16] Kong, L., Chen, G., Zhang, Z., & Wang, H. (2017). Kinematic calibration and investigation of the influence of universal joint errors on accuracy improvement for a 3-DOF parallel manipulator. *Robotics and Computer-Integrated Manufacturing*, *49*, 388–397. https://doi.org/10.1016/j.rcim.2017.08.002

[17] Švaco, M., Šekoranja, B., Šuligoj, F., & Jerbić, B. (2014). Calibration of an industrial robot using a stereo vision system. *Procedia Engineering*, *69*, 459–463. https://doi.org/10.1016/j.proeng.2014.03.012

[18] Li, F., Zeng, Q., Ehmann, K. F., Cao, J., & Li, T. (2018). A calibration method for overconstrained spatial translational parallel manipulators. *Robotics and Computer-Integrated Manufacturing*, *57*, 241–254. https://doi.org/10.1016/j.rcim.2018.12.002

[19] Khalil, W., & Besnard, S. (1999). Self calibration of Stewart-Gough parallel robots without extra sensors. *IEEE Transactions on Robotics and Automation*, *15*(6), 1116–1121. https://doi.org/10.1109/70.817674

[20] Chiu, Y. J., & Perng, M. H. (2003). Self-calibration of a general hexapod manipulator using cylinder constraints. *International Journal of Machine Tools and Manufacture*, *43*, 1051–1066. https://doi.org/10.1016/S0890-6955(03)00082-8

[21] Zhang, B., Zhou, F., Shang, W., & Cong, S. (2019). Auto-Calibration and Online-Adjustment of the Kinematic Uncertainties for Redundantly Actuated Cable-Driven Parallel Robots. In *2019 IEEE 4th International Conference on Advanced Robotics and Mechatronics (ICARM)*. https://doi.org/10.1109/icarm.2019.8833698

[22] Qian, S., Jiang, X., Qian, P., Zi, B., & Zhu, W. (2024). Calibration of static errors and compensation of dynamic errors for cable-driven parallel 3D printer. *Journal of Intelligent & Robotic Systems*, *110*(1). https://doi.org/10.1007/s10846-024-02062-x

[23] Zhang, Y., Liu, Z., Zheng, D., & Cai, C. (2022). The self-calibration method based on grating-rulers used for 6-DOF motion measurement system. *Measurement*, *204*, 111894. https://doi.org/10.1016/j.measurement.2022.111894

[24] Merlet, J.-P. (2004). Solving the Forward Kinematics of a Gough-Type Parallel Manipulator with Interval Analysis. *The International Journal of Robotics Research*, *23*(3), 221–235. https://doi.org/10.1177/0278364904039806

[25] Zhou, W., Chen, W., Liu, H., & Li, X. (2015). A new forward kinematic algorithm for a general Stewart platform. *Mechanism and Machine Theory*, *87*, 177–190. https://doi.org/10.1016/j.mechmachtheory.2015.01.002

[26] Huang, X., Liao, Q., & Wei, S. (2009). Closed-form forward kinematics for a symmetrical 6-6 Stewart platform using algebraic elimination. *Mechanism and Machine Theory*, *45*(2), 327–334. https://doi.org/10.1016/j.mechmachtheory.2009.09.008

[27] Zhao, K., Liu, Z., Cai, C., Bao, F., Tu, C., & Qi, Y. (2023). Design and calibration of the 6-DOF motion tracking system integrated on the Stewart parallel manipulator. *Optics Express*, *32*(1), 287. https://doi.org/10.1364/oe.510804

[28] Bavdekar, V. A., Deshpande, A. P., & Patwardhan, S. C. (2011). Identification of process and measurement noise covariance for state and parameter estimation using extended Kalman filter. *Journal of Process Control*, *21*(4), 585–601. https://doi.org/10.1016/j.jprocont.2011.01.001

[29] Ryaben'kii, V. S., & Tsynkov, S. V. (2006). A Theoretical Introduction to Numerical Analysis. In *Chapman and Hall/CRC eBooks*. https://doi.org/10.1201/9781420011166

[30] Chen, J., Xie, F., Liu, X., & Chong, Z. (2022). Elasto-geometrical calibration of a hybrid mobile robot considering gravity deformation and stiffness parameter errors. *Robotics and Computer-Integrated Manufacturing*, *79*, 102437. https://doi.org/10.1016/j.rcim.2022.102437

[31] Song, S., Dai, X., Huang, Z., & Gong, D. (2020). Load parameter identification for parallel robot manipulator based on extended Kalman filter. *Complexity*, *2020*, 1–12. https://doi.org/10.1155/2020/8816374

Fei Ren received the B.Eng. degree in Optoelectronic Information Science and Engineering from Kaili University China, in 2021. At present, he is studying for a Master's degree at the Department of Electronic and Information Engineering, Guizhou University, Guiyang. His main research interests include robotics and micro vibration calibration.

Zhihua Liu received the B.Eng. degree in Mechanical Engineering from Jilin University, Changchun, China, in 2010, and his Ph.D. degree in the same field from Tsinghua University, Beijing, China, in 2015. He was a visiting scientist at the Physikalisch-technische Bundesanstalt (PTB), Braunschweig, Germany, in 2018. He is currently a vice research fellow at the National Institute of Metrology, China. His research interests include mechanisms and robotics.

Chenguang Cai received his Ph.D. degree in Precision Instrumentation and Mechanics from the School of Instruments Science and Optoelectronic Engineering, Beihang University, Beijing, China, in 2007. From 2007 to 2009, he worked in the Nokia Research Center in Beijing as a postdoct. He is currently a research fellow in the National Institute of Metrology China. He was a visiting scientist in Physikalisch-technische Bundesanstalt (PTB), Germany, in 2016. He is interested in vibration calibration and optics measurement.

Ming Yang received the B.Eng. degree from the Department of Measurement and Control Technology and Instrumentation, Beijing University of Chemical Technology (BUCT), China, in 2014 and his Ph.D. degree from the Department of Control Science and Engineering, BUCT, in 2020. He is currently a distinguished professor with the Department of Automation at the College of Electrical Engineering, Guizhou University, Guiyang, China. His research interests include laser and machine vision detection, and vibration metrology and monitoring.

Han Zhang received the B.Sc. degree in Measurement and Control Technology and Instrumentation from Beijing Jiaotong University, China, in 2018, and the Ph.D. degree in systems engineering from Beihang University, Beijing, China, in 2023. She is currently a postdoc with the Institute of Mechanics and Acoustics of the National Institute of Metrology, Beijing. Her research interests include deep learning, nondestructive testing, and vibration metrology.

Zixiao Ren is a Master's degree holder and Engineer. He graduated from Beijing Jiaotong University, China. His scientific interests focus on vibration measurement. He is actively involved in the technical development of calibration and testing systems. He has participated in national key research programs and National Natural Science Foundation projects.